Cerium molybdate nanocrystals: Microstructural, optical and gas-sensing properties

Fernanda K.F. Oliveira, Anderson A.G. Santiago, Ariadne C. Catto, Luís F. da Silva, Ricardo L. Tranquilin, Elson Longo, Fabiana V. Motta, Mauricio R.D. Bomio

PII: S0925-8388(20)33926-8

DOI: https://doi.org/10.1016/j.jallcom.2020.157562

Reference: JALCOM 157562

To appear in: *Journal of Alloys and Compounds*

Received Date: 28 July 2020

Revised Date: 9 October 2020

Accepted Date: 11 October 2020

Please cite this article as: F.K.F. Oliveira, A.A.G. Santiago, A.C. Catto, Luí.F. da Silva, R.L. Tranquilin, E. Longo, F.V. Motta, M.R.D. Bomio, Cerium molybdate nanocrystals: Microstructural, optical and gas-sensing properties, *Journal of Alloys and Compounds* (2020), doi: https://doi.org/10.1016/j.jallcom.2020.157562.

Cerium Molybdate Nanocrystals: Microstructural, Optical and Gas-Sensing Properties

Fernanda K.F. Oliveira [a]*, Anderson A.G. Santiago[a], Ariadne C. Catto[b], Luís F. da Silva[c], Ricardo L. Tranquilin[b], Elson Longo[b], Fabiana V. Motta[a], Mauricio R.D. Bomio[a]

[a] *LSQM – Laboratory of Chemical Synthesis of Materials – Department of Materials Engineering, Federal University of Rio Grande do Norte – UFRN, P.O. Box 1524, Natal, RN, Brazil*

[b] *LIEC, Department of Chemistry, Federal University of São Carlos, 13565-905, São Carlos, SP, Brazil*

[c] *Laboratory of Nanostructured Multifunctional Materials, Federal University of São Carlos, 13565-905, São Carlos, SP, Brazil*

CRediT authorship contribution statement

Fernanda K.F. Oliveira: Conceptualization, Formal analysis, Writing - review & editing, Visualization. **Anderson A.G. Santiago**: Methodology, Writing - original draft. **Ricardo L. Tranquilin**: Investigation. **Ariadne C. Catto**: Formal analysis, Methodology. **Luís F. da Silva**: Validation, Writing - Review & Editing. **Elson Longo**: Resources. **Fabiana V. Motta**: Supervision. **Mauricio R.D. Bomio**: Supervision, Project administration, Writing - Review & Editing.

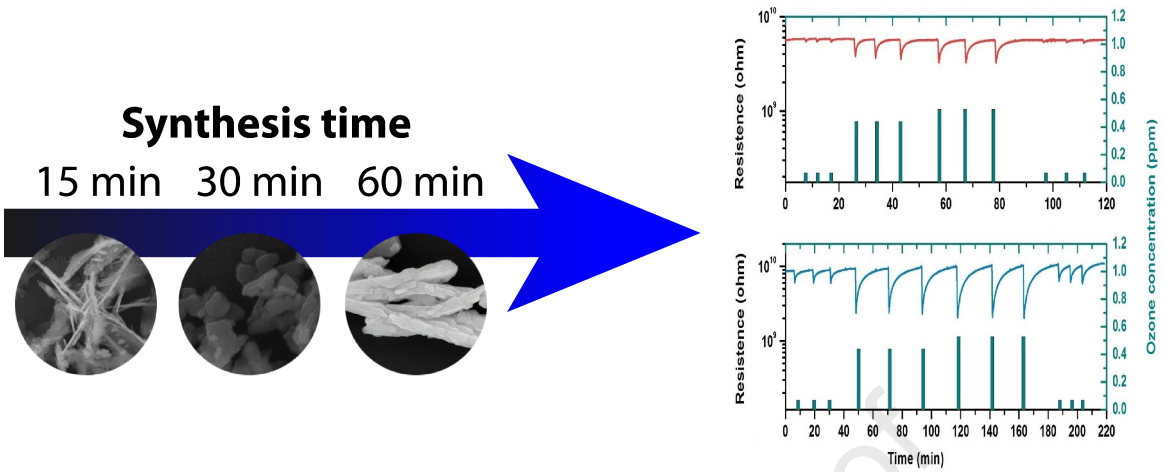

Cerium Molybdate Nanocrystals: Microstructural, Optical and Gas-Sensing Properties

Fernanda K.F. Oliveira [a]*, Anderson A.G. Santiago[a], Ariadne C. Catto[b], Luís F. da Silva[c], Ricardo L. Tranquilin[b], Elson Longo[b], Fabiana V. Motta[a], Mauricio R. D. Bomio[a]

[a] *LSQM – Laboratory of Chemical Synthesis of Materials – Department of Materials Engineering, Federal University of Rio Grande do Norte – UFRN, P.O. Box 1524, Natal, RN, Brazil*

[b] *LIEC – Interdisciplinary Laboratory of Electrochemistry and Ceramics, Department of Chemistry, Federal University of São Carlos, 13565-905, São Carlos, SP, Brazil*

[c] *Laboratory of Nanostructured Multifunctional Materials, Federal University of São Carlos, 13565-905, São Carlos, SP, Brazil*

*Corresponding author. Tel: +55-84-3342-2260; Fax: +55-84-3342-2406 E-mail address: fehk.fonseca@hotmail.com (F.K.F. Oliveira); mauricio.bomio@ct.ufrn.br (M.R.D. Bomio)

Abstract

Metal molybdate compounds have attracted considerable attention due to their technological applications. Herein, we demonstrate the controllable synthesis of cerium molybdate ($Ce_2(MoO_4)_3$) nanocrystals via the co-precipitation method followed by microwave-assisted hydrothermal (MAH) treatment at 150 °C during different times (15, 30 and 60 min). The effect of MAH treatment time on the microstructural, optical, and ozone gas-sensing properties of these nanocrystals was investigated. X-ray diffraction (XRD) and Raman spectroscopy measurements revealed that the samples presented a single-crystalline phase with scheelite-type tetragonal structure. Field emission gun scanning electron microscopy (FEG-SEM) images showed that the MAH conditions favored changes in the $Ce_2(MoO_4)_3$ nanocrystal morphology. Photoluminescence (PL) measurements indicated a significant enhancement of PL emission with MAH time, suggesting an increase in the intrinsic defects formed during the MAH treatment. The gas-sensing performance of cerium molybdate nanocrystals towards sub-ppm ozone levels was also investigated. The experiments revealed complete recovery and good repeatability as well as good sensor response, which was improved in the sample synthesized at longer MAH time.

Keywords: Cerium molybdate; Microwave-assisted hydrothermal; Microstructure; Gas sensor; Ozone.

1. Introduction

Metallic molybdates have aroused interest in several sectors of the industry due to their potential applications in different areas, such as photoluminescence, photocatalysis, and gas sensors [1-7]. In the case of gas-sensing devices, the automotive industry performs daily diverse industrial processes which involve the combustion of fossil fuels, consequently generating several pollutants, such as O_3, CO, NO_x, NH_3, and SO_2 [8, 9]. In the lower atmosphere, these harmful gases cause damage to the environment as well as to human health [10].

Among the harmful pollutants, ozone (O_3) is a strong oxidizing agent used in several practical applications in food industry, water drinking treatment and medical therapies, etc [11-13]. It is formed in the troposphere as a result of photochemical reactions, being related to the pollution generated by vehicles and industrial processes. However, high O_3 gas levels are currently being monitored because of the congestion and inflammation processes which occur when in contact with the human respiratory system [14-16]. To solve this problem, analytical techniques have been used to measure O_3 levels in the range of 0.01 to 10 ppm (parts per million), which are extremely necessary for industrial sensors [17, 18]. These concentrations are required to be detected precisely and rapidly.

Resistive gas sensors are composed of a sensing layer made by semiconducting metal oxide (MOX) or multi-metal oxide (MMO) materials [19, 20]. MOXs have been widely studied due to its simple structure, low cost, and abundance. There are several MOXs described in the literature with potential applications as sensing layers, meanwhile the main MOX used as sensing material in chemical gas sensor devices are SnO_2 [21], ZnO [22], WO_3 [23], In_2O_3 [24], and CuO [25]. These MOXs have presented high sensitivity for different analytes (reducing and oxidizing), good stability, and low production cost, facilitating their integration into sensor devices [8, 26, 27]. As mentioned, MMO nanomaterials (such as

$NaBi(MoO_4)_2$) are another class of materials currently used to improve gas detection because of their adjustable structural, photocatalytic, catalytic, and electrical properties [28]. On the other hand, few papers investigate the gas-sensing performance of MMOs compounds [3, 4].

Among the MMOs, we can highlight $A_2(MoO_4)_3$ molybdates, which belong to the scheelite family and can have tetragonal or monoclinic structures, where A atoms can be La^{3+}, Ce^{3+}, Pr^{3+}, Nd^{3+}, Sm^{3+} and Eu^{3+} [29]. These types of structures can promote complex molybdates and provide high feasibility for incorporating different doping metals, including rare-earth elements [30]. Therefore, rare-earth metal(III) exhibits a tetragonal structure with space group $I4_1/a$, in which the [MoO_4] cluster is coordinated by four oxygen atoms resulting in a polyhedral which can be strongly distorted [31-34] metallic clusters without complete occupancy.

$Ce_2(MoO_4)_3$ nanocrystals are inorganic materials that have received great attention due to their photoluminescent [34], biosensing [35], photonic [34] and catalytic [36, 37] properties, having application in various fields. Several synthesis methods have been used to produce $Ce_2(MoO_4)_3$ nanocrystals, such as organometallic precursors [32], sol-gel [38], and solvothermal [33] and microwave-assisted hydrothermal/solvothermal methods [34]. Singh et al. synthesized cerium molybdate by the hydrothermal method at 180 °C for different times (from 6 to 48 h), using a mixture of water and ethanol as synthesis solvents to obtain the pure phase [35]. In contrast, Maisang et al. synthesized cerium molybdate by the microwave-assisted hydro/solvothermal method and obtained the monoclinic phase [34].

In the present study, we describe the synthesis of $Ce_2(MoO_4)_3$ nanocrystals via a microwave-assisted route and their structural, optical, and gas-sensing properties. To the best of our knowledge, this is the first time that cerium molybdate is used as a sensing material for the detection of sub-ppm ozone levels. The nanocrystals were obtained by the co-precipitation method and then treated in a microwave-assisted hydrothermal (MAH) system at 150 °C for

different times (15, 30, and 60 min). The as-obtained $Ce_2(MoO_4)_3$ nanocrystals were investigated by X-ray diffraction, micro-Raman spectroscopy, ultraviolet-visible spectroscopy, electron microscopies (FEG-SEM and HRTEM), and photoluminescent (PL) measurements. Gas-sensing experiments revealed good sensitivity and repeatability as well as total recovery after consecutive exposures to various O_3 gas levels.

2. Materials and methods

2.1. Synthesis of $Ce_2(MoO_4)_3$ powders

Ammonium molybdate tetrahydrate ($(NH_4)_6Mo_7O_{24}.4H_2O$, 99% purity, Vetec), cerium (III) nitrate hexahydrate, ($Ce(NO_3)_3.6H_2O$, 99% purity, Alfa Aesar) and distilled water were used as precursor materials. The stoichiometric quantities of $(NH_4)_6Mo_7O_{24}.4H_2O$ and $Ce(NO_3)_3.6H_2O$ in a 2:3 ratio of Ce^{+3} and Mo^{+6} were dissolved in 50 mL of distilled water. The solution pH was adjusted to 7 by adding a strong base to increase the hydrolysis rate. The resulting solution was stirred for 30 min. Afterwards, the mixture was transferred to a Teflon reactor and processed by a microwave-assisted hydrothermal system (2.45 GHz, maximum power of 800 W). The microwave-assisted hydrothermal processing was performed at 150 °C for different times: 15, 30, and 60 min. The as-prepared samples were labeled as CeMO15, CeMO30, and CeMO60, respectively. After the microwave-assisted hydrothermal treatment, the solution was naturally cooled down to room temperature. Then, it was washed with distilled water and ethanol several times. Finally, the yellow powders were collected and dried at 100 °C for 24 h.

2.2. Characterizations of $Ce_2(MoO_4)_3$ powders

$Ce_2(MoO_4)_3$ nanocrystals were structurally characterized by X-ray diffraction using a diffractometer (Shimadzu, XRD-7000, with Cu-Kα radiation) in the 2θ range from 10° to 80°

and with a step size of 0.02°/min. The morphological properties and particle size were investigated using field-emission gun scanning electron microscopy (FEG-SEM) (Supra 35-VP, Carl Zeiss, Germany) operated at different magnifications. Transmission electron microscopy (TEM), high-resolution transmission electron microscopy (HRTEM) images, and chemical analysis using energy-dispersive X-ray spectroscopy (EDS) were performed with a FEI TECNAI G2 F20 microscope operating at 200 kV.

Raman measurements were recorded at room temperature using a T-64000 (Jobin-Yvon, France) triple monochromator coupled to a CCD detector. UV-vis absorption spectra were achieved using a UV-2600 (Shimadzu) device in total reflectance mode. Room-temperature photoluminescence (PL) spectra were collected with an ANDOR-Kymera 193i-B1 device using a 355 nm line of a krypton ion laser (Coherent Innova 90 K, USA) in a Mosospec 27 monochromator and a photomultiplier (Hamamatsu R446).

2.3. Gas-sensing measurements

The as-obtained $Ce_2(MoO_4)_3$ samples were dispersed in isopropyl alcohol by an ultrasonic cleaner for 30 min. The suspension was then dripped onto a pre-cleaned Al_2O_3 substrate with interdigitated Pt electrodes [39]. Afterwards, the samples were annealed at 500 °C for 30 min in an electric oven under air atmosphere. The sensor samples were then inserted into a dynamic chamber that allows the control of the operating temperature (up to 350 ^{o}C) and the O_3 gas levels by using mass flow controllers (MFC). Further details regarding the gas-sensing workbench may be found in a previous work [23]. Ozone gas was formed from oxidizing oxygen molecules of dry air by a calibrated pen-ray UV lamp (UVP, model P/N 90-0004-01), which provided concentrations from 0.07 to 0.53 ppm that were verified using a toxic gas detector (ATI, model F12). The total gas flow rate was kept constant at 500 SCCM (Standard Cubic Centimeters per Minute). The applied DC voltage was also kept constant,

while the electrical resistance was monitored using an electrometer (Keithley, model 6514). The sensor response (S) was defined as $S = R_{air}/R_{O3}$, where R_{air} and R_{O3} are the electric resistances of the device exposed to dry air and gas, respectively.

3. Results and discussion

3.1. Structural Analyses

Figure 1 shows the XRD patterns of $Ce_2(MoO_4)_3$ nanocrystals processed at different MAH treatment times. It was observed that all XRD reflections were indexed to the scheelite-type tetragonal structure following the Inorganic Crystal Structure Database (ICSD) card No. 423509 [40]. In addition, the relative intensities and sharp peaks of the XRD measurements indicate that the $Ce_2(MoO_4)_3$ nanocrystals are well crystallized, suggesting an ordered structure over a long range. Nevertheless, the $Ce_2(MoO_4)_3$ compounds synthesized by unequal methods were obtained with the presence of monoclinic phase [32], hydrate form [33], or secondary phases, such as Ce(OH) [34], $Ce_{11}O_{20}$ and Ce_7O_{12} [31], which is in accordance with the literature. The analysis of these results reveals that the preparation of nanocrystals by the MAH method can promote the obtention of the pristine $Ce_2(MoO_4)_3$ phase, even at shorter MAH times.

[Insert Figure 1]

The lattice parameters and unit cell volume were calculated using the General Structure Analysis System (GSAS) with an EXPGUI graphic interface [41] to obtain quantified information regarding the influence of MAH time on the structural properties of $Ce_2(MoO_4)_3$ nanocrystals. Further information on $Ce_2(MoO_4)_3$ nanocrystals was investigated by the Rietveld refinement method using the Inorganic Crystal Structure Database (ICSD) card No. 423509 [40]. These results (**Table 1** and **Figure S1**) demonstrate the high quality of

the refinements with regard to the lattice parameters, cell volume, refinement reliability parameters, and crystalline size, while the microstrain was revealed by statistical fitting parameters *(R_p, RF^2, and χ^2)* [42].

[Insert Table 1]

The refinement results confirm that the $Ce_2(MoO_4)_3$ nanocrystals obtained by the MAH method present a pure tetragonal phase with I41/a space group. Additionally, the obtained results of the lattice parameters and unit cell of $Ce_2(MoO_4)_3$ nanocrytals are in good agreement with the data reported in the ICSD card No. 423509, as shown in **Table 1**. Nevertheless, some variations in such parameters were observed when comparing the $Ce_2(MoO_4)_3$ samples processed by the MAH route and the reference data(ICSD card no. 423509), which can be linked to different types of synthesis methods [40]. Regarding the MAH time, we noted variations in the values of the lattice parameters *a* and *c*, i.e., a reduction in the parameter *a* and an increase in the parameter *c* as a function of MAH time, which implies the stretching of the tetragonal structure indicated by the *c/a* ratio. Likewise, the amount of phase crystallinity and the average crystallite size were also influenced by the MAH time, as seen in **Table 1**.

Figure 2 illustrates a schematic representation of the $Ce_2(MoO_4)_3$ tetragonal unit cell. This was modeled using the CrystalMaker software [43]. **Figure 2** shows that Mo atoms are coordinated to four oxygen atoms and one Mo-O bond path, forming bisphenoidally distorted tetrahedral [MoO_4] clusters, whose bonding angles, labeled as α and β, were slightly distorted in the lattice exhibiting variations as a function of MAH time. As a consequence, the Mo-O bond paths and O-Mo-O angles exhibited small variations between the samples CeMO15 (Mo-O = 1.711 Å (4x), α = 108.6°, and β = 112.3°) and CeMO30 (Mo-O = 1.732 Å (4x), α = 107.5°, and β = 113.4°), while the sample CeMO60 presented a larger distortion (Mo-O = 1.711 Å (4x), α = 112.2°, and β = 104.2°). Such differences can be attributed to the

continuous dissolution and recrystallization process of $Ce_2(MoO_4)_3$ nanocrystals promoted by the MAH processing and treatment time [44].

On the other hand, the site of the Ce^{3+} cations cannot be fully occupied in this structure due to the need to maintain the electroneutrality conditions. Because of this, two-thirds of the Ce atoms are coordinated to eight oxygen atoms and two Ce-O bond paths, thus forming trigonal dodecahedral $[Ce_{0.667}O_8]$ clusters [40, 45-47]. Similar to the Mo-O bond path, the Ce-O bond path exhibited a small difference between the samples CeMO15 (Ce-O = 2.553 Å (4x) and 2.597 Å (4x)) and CeMO30 (Ce-O = 2.533 Å (4x) and 2.581 Å (4x)), while the CeMO60 nanocrystals presented a more expressive distortion (Ce-O = 2.522 Å (4x) and 2.693 Å (4x)). Therefore, the $Ce_2(MoO_4)_3$ sample obtained by the MAH route proved to be extremely sensitive to the synthesis time. In addition, since such structural modifications are strongly influenced by the cluster distortions, they can usually result in improved properties [48].

[Insert Figure 2]

3.2. Raman Spectroscopy

The Raman-active phonon modes are a powerful characterization to investigate and estimate the short-range structural order in the materials [49]. According to the literature [50, 51], the scheelite-type tetragonal structure has 26 different modes in the theoretical calculation ($\Gamma = 3A_g + 5A_u + 5B_g + 3B_u + 5E_g + 5E_u$) for zero wavevectors of the scheelite primitive cell, where 13 vibration modes ($3A_g$, $5B_g$, and $5E_g$) are active in the Raman spectra, while only 8 ($4A_u$ and $4E_u$) are active in the infrared. In contrast, 2 modes (A_u and E_u) are acoustic vibrations and the $3B_u$ vibrations are silent modes.

According to Raman spectroscopy, there are only two vibrational modes in scheelite structures, namely external and internal modes [50, 52]. The first corresponds to the motion of the Ce^{3+} cation and the rigid $[MoO_4]^{2-}$ tetrahedral molecular units, while the second,

considered as the stationary state of the mass center, belongs to the vibration inside $[MoO_4]^{2-}$ tetrahedral units [46, 53]. The $[MoO_4]^{2-}$ tetrahedrons have T_d symmetry in free space [50], and their internal modes are composed by ν_1 (A_1), ν_2 (E_1), ν_3 (F_2) and ν_4 (F_2), one free rotation mode, $\nu_{f.r.}$, (F_1) and one translation mode (F_2) [54].

Figure 3 displays the Raman spectra of the $Ce_2(MoO_4)_3$ nanocrystals in the range of 100 to 1200 cm^{-1}. The spectra clearly show the existence of three bands at 893, 380, and 316 cm^{-1}. In addition, we can observe shifts in the Raman modes of $Ce_2(MoO_4)_3$ caused by the covalent bond formation between Mo^{6+} and O^{2-} ions in the $[MoO_4]$ clusters, which change the efficient mass of the oscillating atoms. This phenomenon can be influenced by some parameters, such as preparation methodology, average crystal size, distortions in the O-Mo-O and O-Ce-O bonds, interaction forces between the ions, or even the degree of structural order in the lattice [55].

The active Raman modes show that the $Ce_2(MoO_4)_3$ nanocrystals are structurally disordered at short range. The analysis of the results reveals the presence of ν_1 (A_g) mode at approximately 893 cm^{-1}, which is associated with the symmetric stretching of the tetrahedral $[MoO_4]$ clusters. The peaks at 824 and 795 cm^{-1} corresponding to ν_3 (B_g) and ν_3 (E_g) modes, respectively, are attributed to the anti-symmetric stretching. At 380 cm^{-1}, a less intense ν_4 (B_g) mode is identified, and the peak at 316 cm^{-1} is a stronger ν_2 (A_g) mode of the regular $[MoO_4]$ cluster [56]. Regarding the MAH time, we also observed an increase in the intensity of the modes as a function of MAH treatment time **(Figure 3)**, revealing an enhancement of structural organization of the $Ce_2(MoO_4)_3$ samples, which is in good agreement with the XRD analyses.

3.3. Morphology of $Ce_2(MoO_4)_3$ nanocrystals

FEG-SEM micrographs of the as-obtained $Ce_2(MoO_4)_3$ nanocrystals are illustrated in **Figure 4**. **Figures 4(a-c)** show that the sample CeMO15 is composed of nanostructured sheets and agglomerated plates, in addition to presenting a polydispersal nature with a random growing without orientation planes. **Figures 4(d-i)** reveal that the samples CeMO30 and CeMO60 are formed by nanoplate and polyhedron-shaped morphology with larger particle sizes when compared to CeMO15, which has a relationship with the crystallite size values seen in **Table 1**. The morphology of the CeMO30 and CeMO60 nanocrystals had a similar shape to that reported by Singh et al. [35] when they synthesized $Ce_2(MoO_4)_3$ at 180 °C for 48 h via the conventional hydrothermal route. Therefore, this morphology tends to be formed in hydrothermal methods in the absence of surfactants.

The morphological variations found in $Ce_2(MoO_4)_3$ nanocrystals can be attributed to the microwave radiation used in the MAH method, which promotes high heating rates, many collisions of atoms, and fast formation of nanoparticles present in the $Ce_2(MoO_4)_3$ precursor solution. Both the MAH treatment time and heating provoke the nucleation of several crystalline nuclei due to microwave radiation penetration. Afterwards, when the nucleus reaches a critical size, it grows to form the particles so that a large number of particles prevents the overgrowth of the others [2, 57]. The MAH method also allows the obtention of crystalline compounds in short synthesis times compared to the conventional hydrothermal route. Since the increase in the synthesis time allowed particle growth and morphology changes, all the events aforementioned can justify the adsorption process between the particles [58-60].

[Insert Figure 4]

Figures 5 (a-f) display the TEM images of the as-obtained samples CeMO15, CeMO30, and CeMO60. It is possible to observe that the CeMO15 particles are quite thin as a

nanosheet on account of their high TEM beam transmittance, resulting in images with translucent particles. However, longer MAH synthesis times promoted the growth of thicker particles due to a lower TEM beam transmittance, consequently enhancing the opacity of the particle image. **Figures 5 (g-i)** show the HR-TEM images of the nanocrystals, where it is possible to see interplanar distances of 0.32, 0.31, and 0.31 nm for CeMO15, CeMO30, and CeMO60, respectively, which correspond to the (112) Miller index. Furthermore, the SAED patterns in **Figures 5 (j-l)** confirm the polycrystalline nature of the as-obtained materials, demonstrated by the diffraction concentric rings of (112), (002), (024), and (116) planes, which could be observed according to their interplanar spacing in the respective figures and **Table 2**. The SAED patterns proved that $Ce_2(MoO_4)_3$ nanocrystals were formed.

[Insert Figure 5]

[Insert Table 2]

EDS analysis was used for the elemental characterization of the $Ce_2(MoO_4)_3$ nanocrystals. Figures 6 (a-c) indicate the presence of the elements O, Ce, and Mo as well as the elements C, Ni, and Cu from the TEM grid.

[Insert Figure 6]

3.4. UV-vis Absorption Spectroscopy Analyses

The optical gap (E_{gap}) was first estimated from the diffuse reflectance data and converted to absorbance through the Kubelka-Munk function [61-63], then calculated by the method proposed by Wood and Tauc [64].

Figure 7 shows the band gap energy for all $Ce_2(MoO_4)_3$ samples, using n = 1/2 (i.e. direct permissible transition) [32, 34]. Each energy gap was determined by extrapolating each linear portion of the curves until $\alpha = 0$. According to our study, the increase of the MAH time was not able to promote the formation of intermediate energy levels between the valence

(VB) and conduction (CB) bands in $Ce_2(MoO_4)_3$ nanocrystals. Moreover, the presence of these energy levels was found to be dependent on the degree of structural order-disorder in the lattice [44].

[Insert Figure 7]

As a result, we could observe that the E_{gap} value ranged between 2.76 and 2.84 eV, which is consistent with the values reported in the literature for the $Ce_2(MoO_4)_3$ compound [32, 34]. These values can then indicate that the samples present a certain degree of order-disorder, which directly influences their structural defects.

3.5. Photoluminescence Analyses

Figures 8 (**a-b)** show the room-temperature photoluminescence (PL) spectra and the CIE (International Commission on Illumination) diagram of the $Ce_2(MoO_4)_3$ nanocrystals, respectively. The result of the PL spectra indicates that all $Ce_2(MoO_4)_3$ nanocrystals exhibit broadband emission with maximum intensity at approximately 500 nm (blue-green region). This behavior can be explained by the multiphonon and multilevel process, where the relaxation process involves many states that participate in several levels within the band gap of the material [65, 66].

[Insert Figure 8]

Several studies in the literature have reported on the possible origin of the PL properties of molybdates, basing their explanations on the recombination of electrons in the $^1T_2$ excited state and holes in the $^1A_1$ ground state [67], the charge transfer transitions within the $[MoO_4]^{2-}$ complex [68], the energy absorption of the 2p orbitals of oxygen and the promotion of molybdenum 4d orbital [69], and vacancies in the oxygen complex $[MoO_4]$ clusters [70].

Figure 8 (a) indicates that the maximum PL emission of the $Ce_2(MoO_4)_3$ nanocrystals are in the blue region and centered around 463, 474, and 483 nm for CeMO15, CeMO30, and CeMO60, respectively, which is generally attributed to a charge diffusion from the Ce 4f level to the O 2p level [71]. As previously mentioned, several authors have tried to determine the mechanism of the PL properties. Using theoretical investigations, our group has proposed that the physical property is directly associated with distortions in the $[MoO_4]$ and $[XO_8]$ clusters (X= Ca, Ba, Pb, Sr) [72]. Therefore, in our study we could observe a substantial increase in the intensity of the PL emission with MAH time. This finding can be related to the degree of order-disorder of the nanocrystals as a function of MAH time, which consequently generated defects that induced symmetry breaking in the material. However, some studies have attributed the increase in the PL spectra to a slightly intrinsic distortion of the tetrahedral $[MoO_4]$ clusters, the morphology, and the charge-transfer transitions within the $[MoO_4]^{2-}$ complex (ions) [45, 70, 73-75]. These distortions are responsible, for example, for the excellent interaction between the Mo atoms and the microwave radiation, and the continuous dissolution and recrystallization mechanisms during the crystal growth processes.

As it can be seen in **Figure 2**, the $[MoO_4]$ clusters created greater distortions in α and β angles, which in turn caused the Mo-O bond paths and O-Mo-O angles to exhibit small variations between the samples CeMO15 (Mo-O = 1.711 Å (4x), α = 108.6°, and β = 112.3°) and CeMO30 (Mo-O = 1.732 Å (4x), α = 107.5°, and β = 113.4°), while the sample CeMO60 presented a larger distortion (Mo-O = 1.711 Å (4x), α = 112.2°, and β = 104.2°). Such distortions in the $Ce_2(MoO_4)_3$ nanoparticles are important for the formation of deep-level defect process and influence the blue PL emission more intensely in CeMO60 due to the longer time of exposure to microwave radiation. This observation was based on the structural refinement data performed for each $Ce_2(MoO_4)_3$ nanocrystal (**Figure 2** and **Table S1**).

3.6. Ozone Gas-Sensing Performance

As previously mentioned, few studies have focused on the gas-sensing performance of molybdates. In one of them, Zou et al. reported the gas-sensing properties of a composite based on $Fe_2(MoO_4)_3$ microspheres for the detection of butanol [4]. With regard to the sensitivity towards ozone (O_3) gas, at the present moment we have not found any study in the literature, justifying our investigation on the ozone gas-sensing properties of $Ce_2(MoO_4)_3$ nanocrystals.

The thermal stability of the tetragonal phase of the powders was measured by thermal treatment at 500 °C for 30 min, and the conservation of such phase after thermal treatment was observed, as it can be seen in **Figure S2.** The optimum operating temperature (T_{opt}) of the $Ce_2(MoO_4)_3$ nanocrystals was initially investigated by varying the T_{opt} from 100 to 350 °C and exposing each sample to 0.07 ppm of O_3 gas for 30 s. According to **Figure 9**, the sensor responses increase with the operating temperature (T_{opt}), reaching a maximum value at approximately 200 °C, and then decrease at higher temperatures. This behavior was identified in both samples (CeMO30 and CeMO60); however, the latter exhibited a higher response at this temperature than the first. This enhancement can be attributed to the presence of additional active sites on the CeMO60 surface, possibly formed as a result of longer MAH synthesis time. We would like to draw attention to the following points: (i) due to the high resistance of the samples, the lowest T_{opt} studied was 100 °C; (ii) the sample CeMO15 did not exhibit any sensitivity towards different O_3 levels, considering the T_{opt} and the gas level range investigated herein.

[Insert Figure 9]

According to the literature, the traditional MOXs used as ozone sensing layer are SnO_2, ZnO, WO_3, and In_2O_3 [13, 76, 77]. These MOXs have been treated at temperatures of

around 150 and 300 ^{o}C. Thus, the working temperature obtained herein for cerium molybdate samples demonstrates its potential as an O_3 sensing layer.

The samples were kept at 200 °C and then exposed to different gas levels (i.e. from 0.07 to 0.53 ppm) in order to investigate the O_3 detection range. As seen in **Figures 10 (a-b)**, the electrical resistance decreases under the presence of different O_3 levels, indicating a p-type conduction behavior [78, 79]. In addition, a gradual enhancement of the sensor response to O_3 concentration can be observed. It should be noted that both samples detected low ozone levels, even after consecutive exposure cycles, highlighting their complete recovery and chemical stability.

Furthermore, the response (t_{resp}) and recovery (t_{rec}) times for both samples were also estimated. The t_{resp} is defined as the time required for the electrical resistance to reach 90% of the initial value when exposed to the analyte investigated, while t_{rec} corresponds to the required time for the electrical resistance to reach 90% of its initial value after the interruption of the analyte flow. The obtained t_{resp} values were similar for all samples, varying from 23-28 s (CeMO30) and 22-25 s (CeMO60) depending on the O_3 level investigated. On the other hand, CeMO30 presented a three times faster recovery than CeMO60, i.e. around 2 and 6 min, respectively. As abovementioned, the high sensitivity of CeMO60 implies a high density of O_3 molecules adsorbed, which require more time for their complete desorption from the sample surface.

[Insert Figure 10]

Additionally, **Figure 10** shows that despite both samples successfully detected sub-ppm levels of O_3 gas, the sample CeMO60 exhibited a higher response, considering the O_3 levels investigated .

A brief summary of the T_{opt} and the minimum O_3 level detected, recently reported for some MOXs synthesized by different methodologies, can be observed in **Table 3**.

[Insert Table 3]

As found in the literature, the superior sensing performance might be attributed to the presence of pre-adsorbed species on the semiconductor surfaces (acting as active sites), morphological features and the crystallization degree, among others [16, 80-82]. Therefore, our findings showed that the MAH treatment time plays an important role in the formation of active sites responsible for the adsorption of ozone molecules. We also observed similar improvements for the $CuWO_4$ compound annealed at different temperatures in conventional oven [61].

4. Conclusions

$Ce_2(MoO_4)_3$ nanocrystals were synthesized by the co-precipitation method and treated at 150 °C in a microwave-assisted hydrothermal system for 15, 30 and 60 min. According to the XRD and Raman results, the as-obtained nanocrystals presented a scheelite-type tetragonal structure without secondary phases. The FEG-SEM and TEM micrographs revealed the presence of crystals exhibiting nanosheet and nanoplate shapes. Regarding the optical properties, UV-vis spectra showed that the optical band gap of cerium molybdates remained unchanged with MAH time. The PL spectrum of the sample CeMO60 (treated for 60 min) exhibited an intense broadband emission in the blue region, which was associated with oxygen vacancies and defects of $[MoO_4]$ and/or $[Ce_{0.667}O_8]$ clusters formed during the MAH treatment. Electrical measurements revealed the ozone sensitivity of $Ce_2(MoO_4)_3$ nanocrystals in the range of 0.07 to 0.53 ppm. The samples presented a good response and total recovery after consecutive exposures, but mainly the one treated for 60 min (CeMO60). This behavior can be linked to the effect of the MAH treatment time, which favored the formation of active sites on the cerium molybdate surface. Finally, the promising properties of cerium molybdates

synthesized via facile and clean route, the MAH method, make them potential candidates for application as sensing layer for the detection of sub-ppm ozone levels.

CRediT authorship contribution statement

Fernanda K.F. Oliveira: Conceptualization, Formal analysis, Writing - Review & Editing, Visualization. **Anderson A.G. Santiago**: Methodology, Writing - Original draft. **Ricardo L. Tranquilin**: Investigation. **Ariadne C. Catto**: Formal analysis, Methodology. **Luís F. da Silva**: Validation, Writing - Review & Editing. **Elson Longo**: Resources. **Fabiana V. Motta**: Supervision. **Mauricio R.D. Bomio**: Supervision, Project administration, Writing - Review & Editing.

Acknowledgments

The authors wish to thank the following Brazilian funding agencies for the financial support: the National Council for Scientific and Technological Development – *CNPq* (under grant number 303657/2017-0), the São Paulo Research Foundation – *FAPESP* (under grant numbers 2013/07296-2 and 2017/12437-5), the Graduate Program in Materials Science and Engineering – *PPGCEM/UFRN*) and the Coordination of Improvement of Higher Education Personnel – *CAPES* (Finance Code 001). The electrodes used for the gas-sensing experiments were fabricated in the Laboratory of Microfabrication at the Brazilian Nanotechnology National Laboratory – *LNNano/CNPEM* (Project LMF-18580). The authors would also like to thank Prof. Maximo Lui for the photoluminescence measurements.

Conflicts of interest

The authors declare that they have no known competing financial interests or personal relationships which could have appeared to influence the work reported in this paper.

References

[1] M. Dargahi, M. Masteri-Farahani, S. Shahsavarifar, M. Feizi, Microemulsion-mediated preparation of $Ce_2(MoO_4)_3$ nanoparticles for photocatalytic degradation of crystal violet in aqueous solution, Environmental Science and Pollution Research, (2020) 1-8.
[2] N.A. Neto, T. Nunes, M. Li, E. Longo, M. Bomio, F. Motta, Influence of microwave-assisted hydrothermal treatment time on the crystallinity, morphology and optical properties of $ZnWO_4$ nanoparticles: Photocatalytic activity, Ceramics International, 46 (2020) 1766-1774.
[3] S. Zou, J. Luo, Z. Lin, P. Fu, Z. Chen, Acetone gas sensor based on iron molybdate nanoparticles prepared by hydrothermal method with PVP as surfactant, Materials Research Express, 5 (2018) 125013.
[4] S. Zou, J. Gao, L. Liu, Z. Lin, P. Fu, S. Wang, Z. Chen, Enhanced gas sensing properties at low working temperature of iron molybdate/MXene composite, Journal of Alloys and Compounds, 817 (2020) 152785.
[5] Z. Shahri, M. Bazarganipour, M. Salavati-Niasari, Controllable synthesis of novel zinc molybdate rod-like nanostructures via simple surfactant-free precipitation route, Superlattices and Microstructures, 63 (2013) 258-266.
[6] G. Kianpour, F. Soofivand, M. Badiei, M. Salavati-Niasari, M. Hamadanian, Facile synthesis and characterization of nickel molybdate nanorods as an effective photocatalyst by co-precipitation method, Journal of Materials Science: Materials in Electronics, 27 (2016) 10244-10251.
[7] M.S. Morassaei, A. Salehabadi, M. Salavati-Niasari, A. Akbari, Preparation, structural analysis, and assessing the impacts of holmium and ytterbium on electrochemical hydrogen storage property of strontium cerium molybdate nanostructures, Electrochimica Acta, 356 (2020) 136851.
[8] Y.J. Onofre, A.C. Catto, S. Bernardini, T. Fiorido, K. Aguir, E. Longo, V.R. Mastelaro, L.F. da Silva, M.P. de Godoy, Highly selective ozone gas sensor based on nanocrystalline $Zn_{0.95}Co_{0.05}O$ thin film obtained via spray pyrolysis technique, Applied Surface Science, 478 (2019) 347-354.
[9] M. Mladenović, M. Paprika, A. Marinković, Denitrification techniques for biomass combustion, Renewable and Sustainable Energy Reviews, 82 (2018) 3350-3364.
[10] G. Singh, A. Kushwaha, M. Sharma, Persistent peroxidase mimics of graphene oxide anchored cerium molybdate sensor: An effective colorimetric detection of S^{2-} and Sn^{2+} ions, Microchemical Journal, 153 (2020) 104290.
[11] R. Toita, K. Tsuru, K. Ishikawa, Ozone-gas-mediated surface hydrophilization enhances the cell responses to titanium, Materials Letters, 261 (2020) 127168.
[12] N. Joshi, L.F. da Silva, H. Jadhav, J.-C. M'Peko, B.B.M. Torres, K. Aguir, V.R. Mastelaro, O.N. Oliveira, One-step approach for preparing ozone gas sensors based on hierarchical $NiCo_2O_4$ structures, RSC advances, 6 (2016) 92655-92662.

[13] L.F. Da Silva, A.C. Catto, W. Avansi, L.S. Cavalcante, J. Andrés, K. Aguir, V.R. Mastelaro, E. Longo, A novel ozone gas sensor based on one-dimensional (1D) α-Ag_2WO_4 nanostructures, Nanoscale, 6 (2014) 4058-4062.
[14] K.C. Abe, S.G.E.K. Miraglia, Health impact assessment of air pollution in São Paulo, Brazil, International journal of environmental research and public health, 13 (2016) 694.
[15] W. Avansi Jr, A.C. Catto, L.i.F. da Silva, T. Fiorido, S. Bernardini, V.R. Mastelaro, K. Aguir, R. Arenal, One-dimensional V_2O_5/TiO_2 heterostructures for chemiresistive ozone sensors, ACS Applied Nano Materials, 2 (2019) 4756-4764.
[16] A.C. Catto, L.s.F.d. Silva, M.I.s.B. Bernardi, S. Bernardini, K. Aguir, E. Longo, V.R. Mastelaro, Local Structure and Surface Properties of $Co_xZn_{1-x}O$ Thin Films for Ozone Gas Sensing, ACS applied materials & interfaces, 8 (2016) 26066-26072.
[17] D. Ziegler, P. Palmero, J.-M. Tulliani, W-doped indium oxide synthetized via hydrothermal route for low-temperature ozone sensing, Solid State Ionics, 347 (2020) 115271.
[18] G. Korotcenkov, V. Brinzari, B. Cho, In_2O_3-and SnO_2-based thin film ozone sensors: fundamentals, Journal of Sensors, 2016 (2016).
[19] S. Davoudi, M.H. Givianrad, M. Saber-Tehrani, P.A. Azar, A novel electrochemical sensor based on Co_3O_4-CeO_2-ZnO multi metal oxide nanocomposite for simultaneous detection of nanomolar Pb2+ and Hg2+ in different kind of spices, (2019).
[20] J. Burgués, S. Marco, Low power operation of temperature-modulated metal oxide semiconductor gas sensors, Sensors, 18 (2018) 339.
[21] G. Korotcenkov, I. Blinov, M. Ivanov, J. Stetter, Ozone sensors on the base of SnO_2 films deposited by spray pyrolysis, Sensors and Actuators B: Chemical, 120 (2007) 679-686.
[22] A.C. Catto, L.F. da Silva, C. Ribeiro, S. Bernardini, K. Aguir, E. Longo, V.R. Mastelaro, An easy method of preparing ozone gas sensors based on ZnO nanorods, Rsc advances, 5 (2015) 19528-19533.
[23] J. Guerin, M. Bendahan, K. Aguir, A dynamic response model for the WO_3-based ozone sensors, Sensors and Actuators B: Chemical, 128 (2008) 462-467.
[24] G. Korotcenkov, A. Cerneavschi, V. Brinzari, A. Vasiliev, M. Ivanov, A. Cornet, J. Morante, A. Cabot, J. Arbiol, In_2O_3 films deposited by spray pyrolysis as a material for ozone gas sensors, Sensors and Actuators B: Chemical, 99 (2004) 297-303.
[25] Y. Wang, F. Qu, J. Liu, Y. Wang, J. Zhou, S. Ruan, Enhanced H_2S sensing characteristics of CuO-NiO core-shell microspheres sensors, Sensors and Actuators B: Chemical, 209 (2015) 515-523.
[26] J. Yang, P. Fu, Z. Lin, Preparation of $KBi(MoO_4)_2$ nanocrystallite by solvothermal process and its gas-sensing properties, Materials Research Express, 5 (2018) 065033.
[27] C. Zhu, W. Guo, F. Du, P. Fu, Q. Deng, Z. Lin, One-pot synthesis of $NaBi(MoO_4)_2$ nanorods and their gas-sensing properties, Materials Letters, 220 (2018) 172-174.
[28] Z. Gao, S. Xie, B. Zhang, X. Qiu, F. Chen, Ultrathin Mg-Al layered double hydroxide prepared by ionothermal synthesis in a deep eutectic solvent for highly effective boron removal, Chemical Engineering Journal, 319 (2017) 108-118.
[29] K. Gaur, M. Singh, H. Lal, Electrical transport in light rare-earth molybdates, Journal of materials science, 28 (1993) 3816-3822.

[30] V.V. Atuchin, A. Aleksandrovsky, O. Chimitova, C.-P. Diao, T. Gavrilova, V. Kesler, M. Molokeev, A. Krylov, B. Bazarov, J. Bazarova, Electronic structure of β-$RbSm(MoO_4)_2$ and chemical bonding in molybdates, Dalton Transactions, 44 (2015) 1805-1815.
[31] P. Klevtsov, R. Klevtsova, Polymorphism of the double molybdates and tungstates of mono-and trivalent metals with the composition $M^+R^{3+}(EO_4)_2$, Journal of Structural Chemistry, 18 (1977) 339-355.
[32] M.S. Sena, A.G.d. Santos, A.L. Lopes-Moriyama, C.P.d. Souza, Synthesis and characterization of cerium molybdate semiconductor nanoparticles, Materials Research, 20 (2017) 485-491.
[33] S. Ayni, M. Sabet, M. Salavati-Niasari, M. Hamadanian, Synthesis and characterization of cerium molybdate nanostructures via a simple solvothermal method and investigation of their photocatalytic activity, Journal of Materials Science: Materials in Electronics, 27 (2016) 7342-7352.
[34] W. Maisang, A. Phuruangrat, S. Thongtem, T. Thongtem, Photoluminescence and photonic absorbance of $Ce_2(MoO_4)_3$ nanocrystal synthesized by microwave–hydrothermal/solvothermal method, Rare Metals, 37 (2018) 868-874.
[35] G. Singh, A. Kushwaha, M. Sharma, Intriguing peroxidase-mimic for H_2O_2 and glucose sensing: A synergistic $Ce_2(MoO_4)_3$/rGO nanocomposites, Journal of Alloys and Compounds, 825 (2020) 154134.
[36] W. Kuang, Y. Fan, Y. Chen, Catalytic properties of ultrafine molybdenum-cerium oxide particles prepared by the sol-gel method, Catalysis letters, 50 (1998) 31-35.
[37] R. Sundaram, K. Nagaraja, Solid state electrical conductivity and humidity sensing studies on metal molybdate–molybdenum trioxide composites (M= Ni^{2+}, Cu^{2+} and Pb^{2+}), Sensors and Actuators B: Chemical, 101 (2004) 353-360.
[38] W. Kuang, Y. Fan, K. Yao, Y. Chen, Preparation and characterization of ultrafine rare earth molybdenum complex oxide particles, Journal of Solid State Chemistry, 140 (1998) 354-360.
[39] L.F. da Silva, J.-C. M'peko, A.C. Catto, S. Bernardini, V.R. Mastelaro, K. Aguir, C. Ribeiro, E. Longo, UV-enhanced ozone gas sensing response of ZnO-SnO_2 heterojunctions at room temperature, Sensors and Actuators B: Chemical, 240 (2017) 573-579.
[40] T. Schustereit, S.L. Müller, T. Schleid, I. Hartenbach, Defect scheelite-type lanthanoid (III) ortho-oxomolybdates (VI) $Ln_{0.667}[MoO_4]$(Ln= Ce, Pr, Nd, and Sm) and their relationship to zircon and the NaTl-type structure, Crystals, 1 (2011) 244-253.
[41] B.H. Toby, EXPGUI, a graphical user interface for GSAS, Journal of applied crystallography, 34 (2001) 210-213.
[42] R. Roca, J. Sczancoski, I. Nogueira, M. Fabbro, H. Alves, L. Gracia, L.S. Santos, C. De Sousa, J. Andrés, G. Luz, Facet-dependent photocatalytic and antibacterial properties of α-Ag_2WO_4 crystals: combining experimental data and theoretical insights, Catalysis Science & Technology, 5 (2015) 4091-4107.
[43] D.C. Palmer, Visualization and analysis of crystal structures using CrystalMaker software, Zeitschrift für Kristallographie-Crystalline Materials, 230 (2015) 559-572.
[44] J. Sczancoski, M. Bomio, L. Cavalcante, M. Joya, P. Pizani, J.A. Varela, E. Longo, M.S. Li, J. Andrés, Morphology and blue photoluminescence emission of $PbMoO_4$ processed in conventional hydrothermal, The Journal of Physical Chemistry C, 113 (2009) 5812-5822.

[45] G. Botelho, I. Nogueira, E. Moraes, E. Longo, Study of structural and optical properties of $CaMoO_4$ nanoparticles synthesized by the microwave-assisted solvothermal method, Materials Chemistry and Physics, 183 (2016) 110-120.
[46] T. Thongtem, S. Kungwankunakorn, B. Kuntalue, A. Phuruangrat, S. Thongtem, Luminescence and absorbance of highly crystalline $CaMoO_4$, $SrMoO_4$, $CaWO_4$ and $SrWO_4$ nanoparticles synthesized by co-precipitation method at room temperature, Journal of Alloys and Compounds, 506 (2010) 475-481.
[47] Y. Ni, J.M. Hughes, A.N. Mariano, Crystal chemistry of the monazite and xenotime structures, American Mineralogist, 80 (1995) 21-26.
[48] M. Almeida, L. Cavalcante, C. Morilla-Santos, C. Dalmaschio, S. Rajagopal, M.S. Li, E. Longo, Effect of partial preferential orientation and distortions in octahedral clusters on the photoluminescence properties of $FeWO_4$ nanocrystals, CrystEngComm, 14 (2012) 7127-7132.
[49] E. Tavares, P. Pizani, J. Eiras, Short-range disorder in lanthanum-doped lead titanate ceramics probed by Raman scattering, Applied physics letters, 72 (1998) 897-899.
[50] T. Basiev, A. Sobol, Y.K. Voronko, P. Zverev, Spontaneous Raman spectroscopy of tungstate and molybdate crystals for Raman lasers, Optical Materials, 15 (2000) 205-216.
[51] F. Oliveira, M. Oliveira, L. Gracia, R. Tranquilin, C. Paskocimas, F. Motta, E. Longo, J. Andrés, M. Bomio, Experimental and theoretical study to explain the morphology of $CaMoO_4$ crystals, Journal of Physics and Chemistry of Solids, 114 (2018) 141-152.
[52] T. Thongtem, A. Phuruangrat, S. Thongtem, Characterization of $MMoO_4$ (M = Ba, Sr and Ca) with different morphologies prepared using a cyclic microwave radiation, Materials Letters, 62 (2008) 454-457.
[53] T. Thongtem, A. Phuruangrat, S. Thongtem, Characterization of $MeWO_4$ (Me= Ba, Sr and Ca) nanocrystallines prepared by sonochemical method, Applied Surface Science, 254 (2008) 7581-7585.
[54] A. Jayaraman, B. Batlogg, L. VanUitert, High-pressure Raman study of alkaline-earth tungstates and a new pressure-induced phase transition in $BaWO_4$, Physical Review B, 28 (1983) 4774.
[55] J. Sczancoski, L. Cavalcante, M. Joya, J.A. Varela, P. Pizani, E. Longo, $SrMoO_4$ powders processed in microwave-hydrothermal: Synthesis, characterization and optical properties, Chemical Engineering Journal, 140 (2008) 632-637.
[56] G. Xing, H. Guo, Z. Yang, C. Yu, Y. Li, Z. Wu, C. Zhao, Controllable synthesis and photocatalytic properties of spherical and flower-like $Ce_2(MoO_4)_3$ hierarchical architectures, Materials Research Innovations, 20 (2016) 272-279.
[57] A.A. Santiago, R.L. Tranquilin, M.C. Oliveira, R.A.P. Ribeiro, S.R. de Lazaro, M.A. Correa, F. Bohn, E. Longo, F.V. Motta, M.R.D. Bomio, Disclosing the Structural, Electronic, Magnetic, and Morphological Properties of $CuMnO_2$: A Unified Experimental and Theoretical Approach, The Journal of Physical Chemistry C, 124 (2020) 5378-5388.
[58] L.S. Cavalcante, J.C. Sczancoski, R.L. Tranquilin, J.A. Varela, E. Longo, M.O. Orlandi, Growth mechanism of octahedron-like $BaMoO_4$ microcrystals processed in microwave-hydrothermal: Experimental observations and computational modeling, Particuology, 7 (2009) 353-362.
[59] S.A. Mousavi, M. Hassanpour, M. Salavati-Niasari, H. Safardoust-Hojaghan, M. Hamadanian, Dy_2O_3/CuO nanocomposites: microwave assisted synthesis and investigated

photocatalytic properties, Journal of Materials Science: Materials in Electronics, 29 (2018) 1238-1245.
[60] F. Namvar, F. Beshkar, M. Salavati-Niasari, Novel microwave-assisted synthesis of leaf-like $MnMoO_4$ nanostructures and investigation of their photocatalytic performance, Journal of Materials Science: Materials in Electronics, 28 (2017) 7962-7968.
[61] L. Tolvaj, K. Mitsui, D. Varga, Validity limits of Kubelka–Munk theory for DRIFT spectra of photodegraded solid wood, Wood Science and Technology, 45 (2011) 135-146.
[62] N. Tavker, M. Sharma, Designing of waste fruit peels extracted cellulose supported molybdenum sulfide nanostructures for photocatalytic degradation of RhB dye and industrial effluent, Journal of Environmental Management, 255 (2020) 109906.
[63] S.B. Vuggili, S.K. Khanth, K. Kadiya, U.K. Gaur, M. Sharma, Improvement in visible light stimulated photocatalysis by the inducement of magnesium dopant inside graphitic carbon nitride frameworks, Journal of Environmental Chemical Engineering, 7 (2019) 103440.
[64] D. Wood, J. Tauc, Weak absorption tails in amorphous semiconductors, Physical Review B, 5 (1972) 3144.
[65] A. Santiago, C. Almeida, R. Tranquilin, R. Nascimento, C. Paskocimas, E. Longo, F. Motta, M. Bomio, Photoluminescent properties of the $Ba_{1-x}Zn_xMoO_4$ heterostructure obtained by ultrasonic spray pyrolysis, Ceramics International, 44 (2018) 3775-3786.
[66] V. Longo, L.d. Cavalcante, A. De Figueiredo, L. Santos, E. Longo, J.A. Varela, J. Sambrano, C. Paskocimas, F. De Vicente, A. Hernandes, Highly intense violet-blue light emission at room temperature in structurally disordered $SrZrO_3$ powders, Applied Physics Letters, 90 (2007) 091906.
[67] A. Phuruangrat, T. Thongtem, S. Thongtem, Preparation, characterization and photoluminescence of nanocrystalline calcium molybdate, Journal of alloys and compounds, 481 (2009) 568-572.
[68] C.S. Lim, Microwave-assisted synthesis and photoluminescence of $MMoO_4$ (M= Ca, Ba) particles via a metathetic reaction, Journal of luminescence, 132 (2012) 1774-1780.
[69] V. Marques, L. Cavalcante, J. Sczancoski, A. Alcântara, M.O. Orlandi, E. Moraes, E. Longo, J.A. Varela, M. Siu Li, M. Santos, Effect of different solvent ratios (water/ethylene glycol) on the growth process of $CaMoO_4$ crystals and their optical properties, Crystal Growth & Design, 10 (2010) 4752-4768.
[70] V.M. Longo, A.T.d. Figueiredo, A.B. Campos, J.W. Espinosa, A.C. Hernandes, C. Taft, J.R. Sambrano, J.A. Varela, E. Longo, Different origins of green-light photoluminescence emission in structurally ordered and disordered powders of calcium molybdate, The Journal of Physical Chemistry A, 112 (2008) 8920-8928.
[71] J. Saranya, K.S. Ranjith, P. Saravanan, D. Mangalaraj, R.T.R. Kumar, Cobalt-doped cerium oxide nanoparticles: enhanced photocatalytic activity under UV and visible light irradiation, Materials science in semiconductor processing, 26 (2014) 218-224.
[72] C. Almeida, L. Lovisa, A. Santiago, M. Li, E. Longo, C. Paskocimas, F. Motta, M. Bomio, One-step synthesis of $CaMoO_4:Eu^{3+}$ nanospheres by ultrasonic spray pyrolysis, Journal of Materials Science: Materials in Electronics, 28 (2017) 16867-16879.

[73] J.H. Ryu, J.-W. Yoon, C.S. Lim, W.-C. Oh, K.B. Shim, Microwave-assisted synthesis of $CaMoO_4$ nano-powders by a citrate complex method and its photoluminescence property, Journal of alloys and compounds, 390 (2005) 245-249.
[74] Y. Xiang, J. Song, G. Hu, Y. Liu, Synthesis of $CaMoO_4$ hierarchical structures via a simple slow-release co-precipitation method, Applied Surface Science, 349 (2015) 374-379.
[75] X. Liu, L. Li, H.M. Noh, S.H. Park, J.H. Jeong, H.K. Yang, K. Jang, D.S. Shin, Synthesis and photoluminescence of novel 3D flower-like $CaMoO_4$ architectures hierarchically self-assembled with tetragonal bipyramid nanocrystals, Optical Materials, 43 (2015) 10-17.
[76] G. Korotcenkov, B. Cho, Spray pyrolysis deposition of undoped SnO2 and In_2O_3 films and their structural properties, Progress in Crystal Growth and Characterization of Materials, 63 (2017) 1-47.
[77] K. Aguir, C. Lemire, D. Lollman, Electrical properties of reactively sputtered WO_3 thin films as ozone gas sensor, Sensors and actuators B: Chemical, 84 (2002) 1-5.
[78] A. Bejaoui, J. Guerin, J. Zapien, K. Aguir, Theoretical and experimental study of the response of CuO gas sensor under ozone, Sensors and actuators B: chemical, 190 (2014) 8-15.
[79] N. Joshi, L.F. da Silva, H.S. Jadhav, F.M. Shimizu, P.H. Suman, J.-C. M'Peko, M.O. Orlandi, J.G. Seo, V.R. Mastelaro, O.N. Oliveira Jr, Yolk-shelled $ZnCo_2O_4$ microspheres: Surface properties and gas sensing application, Sensors and Actuators B: Chemical, 257 (2018) 906-915.
[80] A.C. Catto, T. Fiorido, É.L. Souza, W. Avansi Jr, J. Andres, K. Aguir, E. Longo, L.S. Cavalcante, L.F. Da Silva, Improving the ozone gas-sensing properties of $CuWO_4$ nanoparticles, Journal of Alloys and Compounds, 748 (2018) 411-417.
[81] L.F. da Silva, V.R. Mastelaro, A.C. Catto, C.A. Escanhoela Jr, S. Bernardini, S.C. Zílio, E. Longo, K. Aguir, Ozone and nitrogen dioxide gas sensor based on a nanostructured $SrTi_{0.85}Fe_{0.15}O_3$ thin film, Journal of Alloys and Compounds, 638 (2015) 374-379.
[82] L.F. Da Silva, J.-C. M'Peko, J. Andres, A. Beltran, L. Gracia, M.I. Bernardi, A. Mesquita, E. Antonelli, M.L. Moreira, V.R. Mastelaro, Insight into the effects of Fe addition on the local structure and electronic properties of $SrTiO_3$, The Journal of Physical Chemistry C, 118 (2014) 4930-4940.
[83] X. Xu, M.A.P. Yazdi, J.-B. Sanchez, A. Billard, F. Berger, N. Martin, Exploiting the dodecane and ozone sensing capabilities of nanostructured tungsten oxide films, Sensors and Actuators B: Chemical, 266 (2018) 773-783.
[84] L. Rocha, C. Foschini, C. Silva, E. Longo, A. Simões, Novel ozone gas sensor based on ZnO nanostructures grown by the microwave-assisted hydrothermal route, Ceramics international, 42 (2016) 4539-4545.
[85] J. Huang, X. Wang, Y. Gong, Y. Liu, P. Zhou, X. Suo, D. Zeng, H. Li, Construction of WO_3 coatings with micro-nano hybrid structures by liquid precursor flame spray for enhanced sensing performances to sub-ppm ozone, Materials Letters, 205 (2017) 106-109.
[86] Y.-T. Tsai, S.-J. Chang, I.-T. Tang, Y.-J. Hsiao, L.-W. Ji, High density novel porous ZnO nanosheets based on a microheater chip for ozone sensors, IEEE Sensors Journal, 18 (2018) 5559-5565.

Table Caption

Table 1. Crystallographic parameters obtained from Rietveld refinement of $Ce_2(MoO_4)_3$ samples

Table 2. d-spacing values and Miller indices of $Ce_2(MoO_4)_3$ nanocrystals compared to ICSD-423509 (Å)

Table 3. Results of ozone gas-sensing performance of compounds synthesized by different methodologies

Table 1.

Compounds	CeMO15	CeMO30	CeMO60	ICSD-423509
Crystal system	Tetragonal	Tetragonal	Tetragonal	Tetragonal
Space group	$I4_1/a$	$I4_1/a$	$I4_1/a$	$I4_1/a$
Lattice parameters (Å)				
A	5.329	5.327	5.324	5.331
C	11.72	11.72	11.73	11.83
c/*a*	2.199	2.201	2.203	2.219
V (Å^3)	332.7	332.6	332.4	336.3
χ^2	1.562	1.439	2.101	-
Rp (%)	11.19	11.05	11.33	-
RF^2 (%)	8.03	6.01	15.88	-
D_{hkl} (nm)	19	21	36	-
ε_{hkl} (x10^{-3})	0.94	0.81	0.49	-

a and *c* are lattice parameters, V is the unit cell volume, D_{hkl} is the average crystallite size, and ε_{hkl} is the microstrain

Table 2.

Miller indices	d-spacing (Å)			
	CeMO15	CeMO30	CeMO60	ICSD 423509
(112)	3.126	3.105	3.153	3.179
(020)	2.671	2.613	2.603	2.665
(024)	2.149	2.087	2.096	1.980
(116)	1.736	1.718	1.721	1.747

Table 3.

Material	Preparation method	Operating temperature (^oC)	Minimum O_3 level detected (ppb)	Reference
$Zn_{0.95}Co_{0.05}O$	Spray pyrolysis	250	20	[8]
$CuWO_4$	Sonochemical route	250	80	[80]
WO_3	DC-magnetron Sputtering	250	200	[83]
ZnO	Microwave-assisted hydrothermal	200	100	[84]
WO_3	Liquid precursor flame spray (LPFS)	150	500	[85]
V_2O_5	Hydrothermal	300	1250	[15]
ZnO	Hydrothermal	300	100	[86]
CeMO	Microwave-assisted hydrothermal	200	70	Present study

Figures Caption

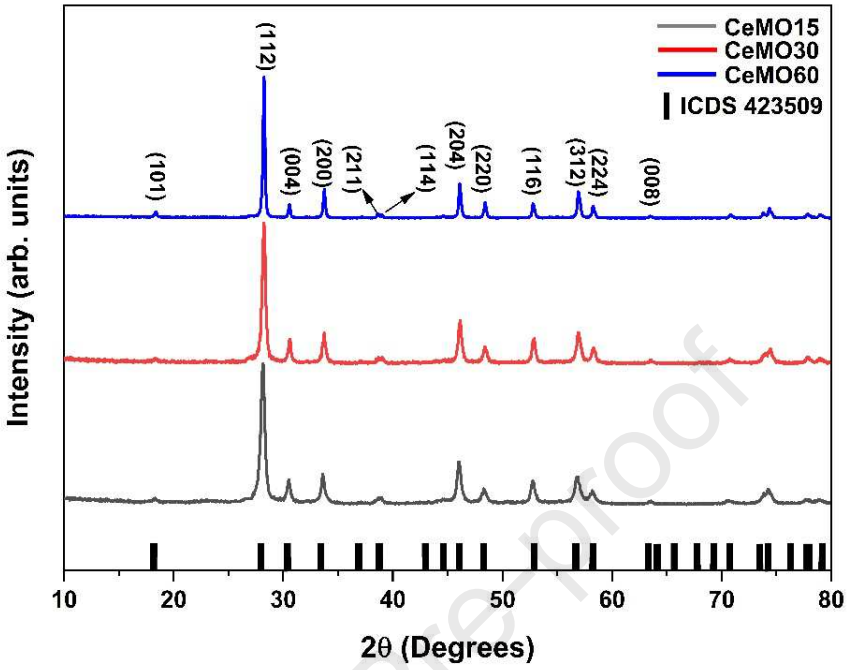

<Fig. 1>

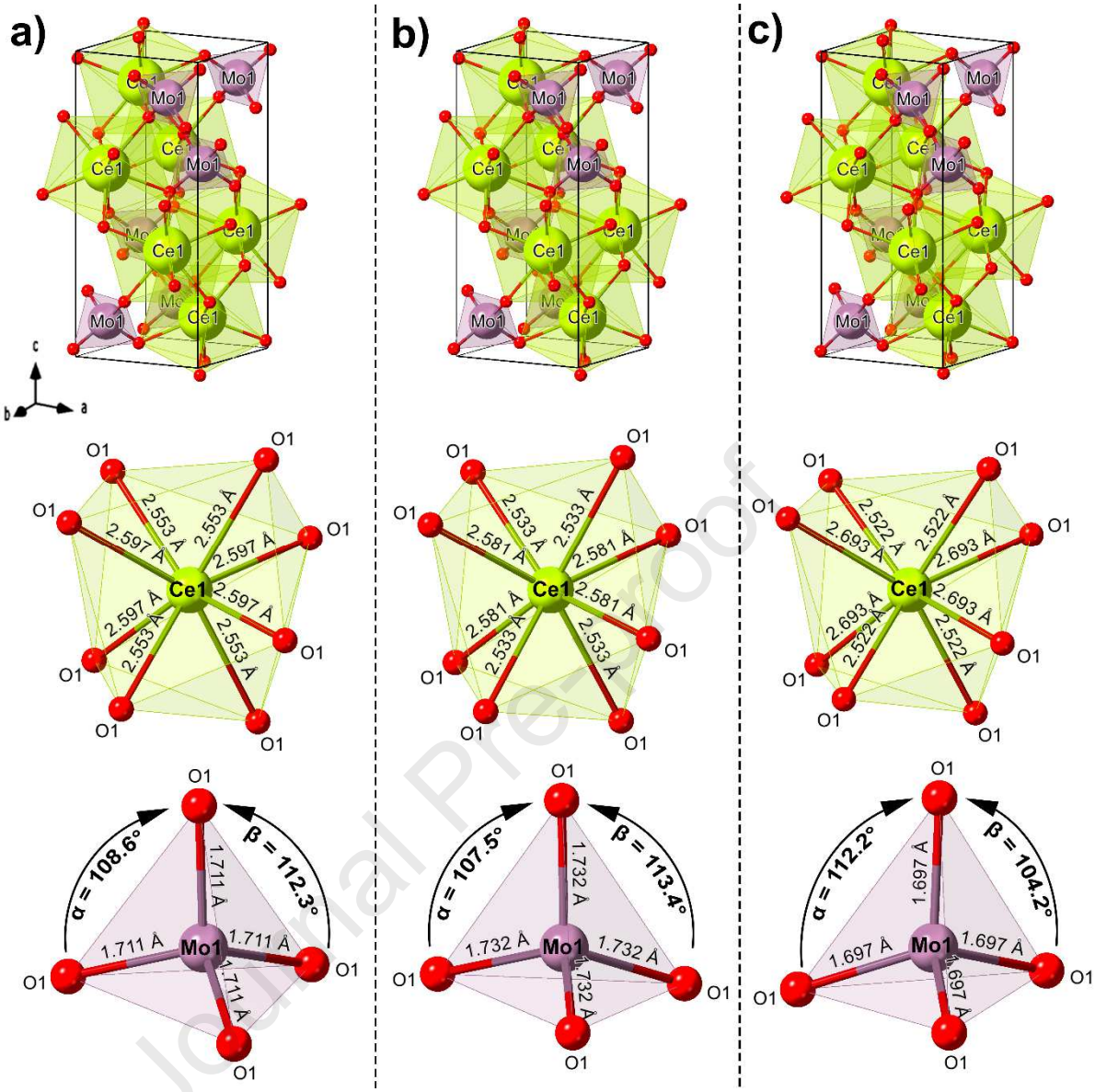

<Fig. 2>

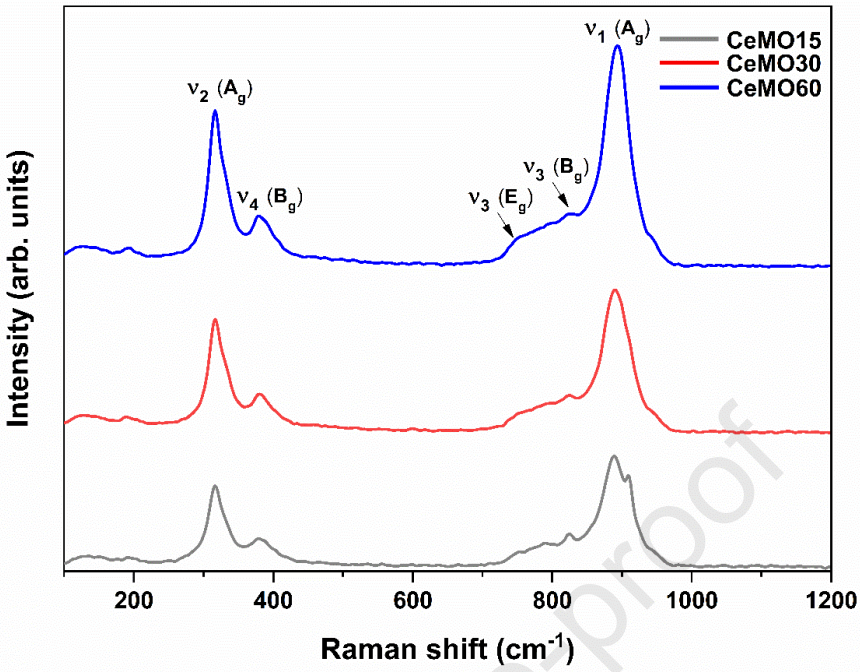

<Fig. 3>

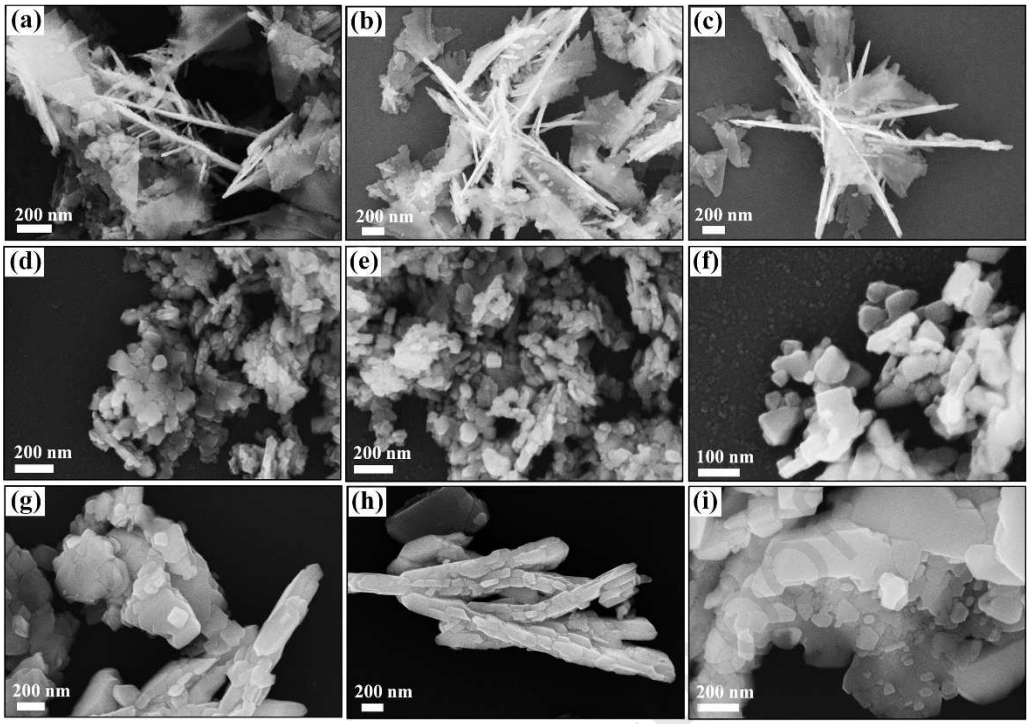

<Fig. 4>

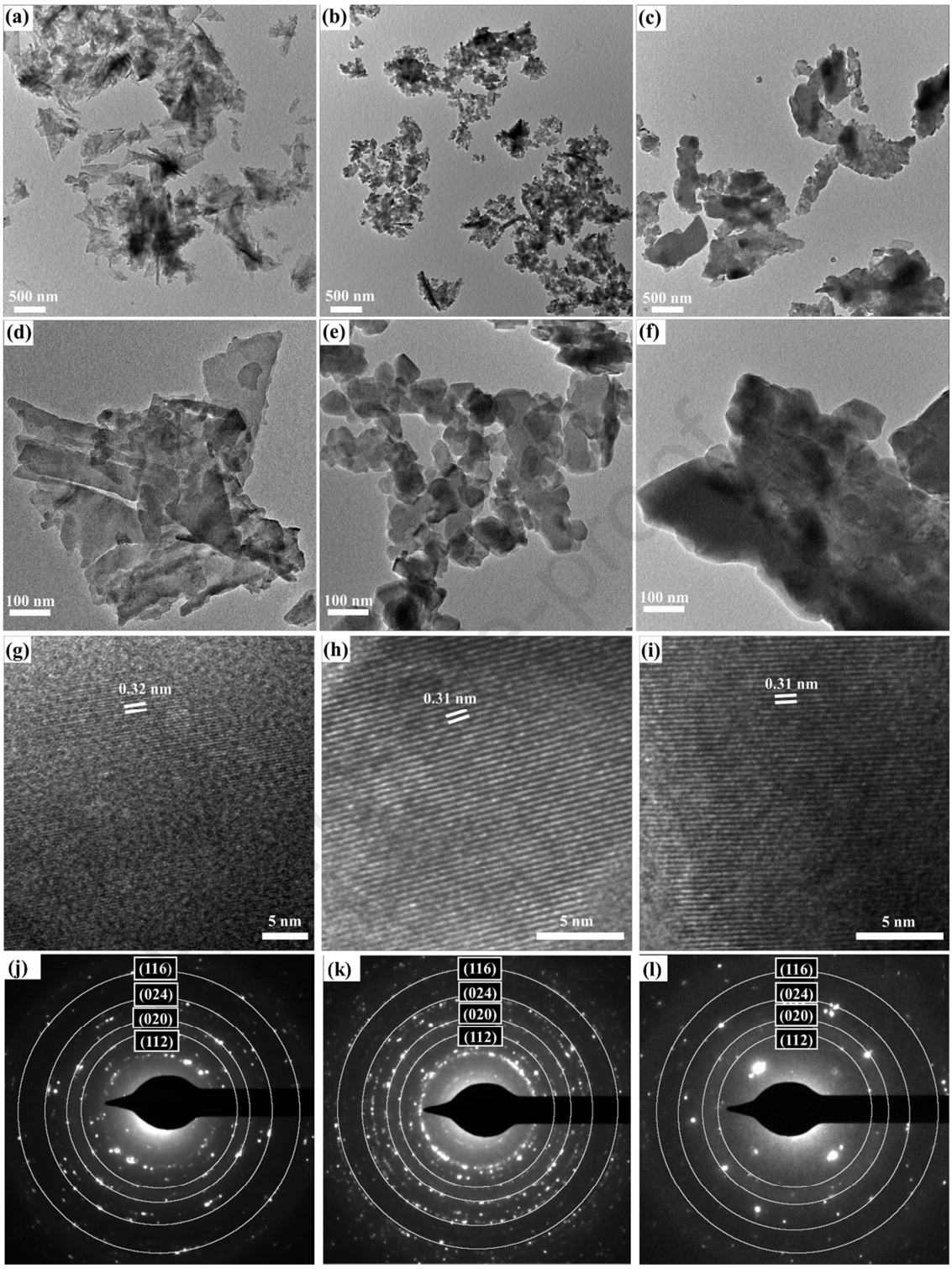
(a)
500 nm
(b)
500 nm
(c)
500 nm
(d)
100 nm
(e)
100 nm
(f)
100 nm
(g)
0.32 nm
5 nm
(h)
0.31 nm
5 nm
(i)
0.31 nm
5 nm
(j)
(116)
(024)
(020)
(112)
(k)
(116)
(024)
(020)
(112)
(l)
(116)
(024)
(020)
(112)

<Fig. 5>

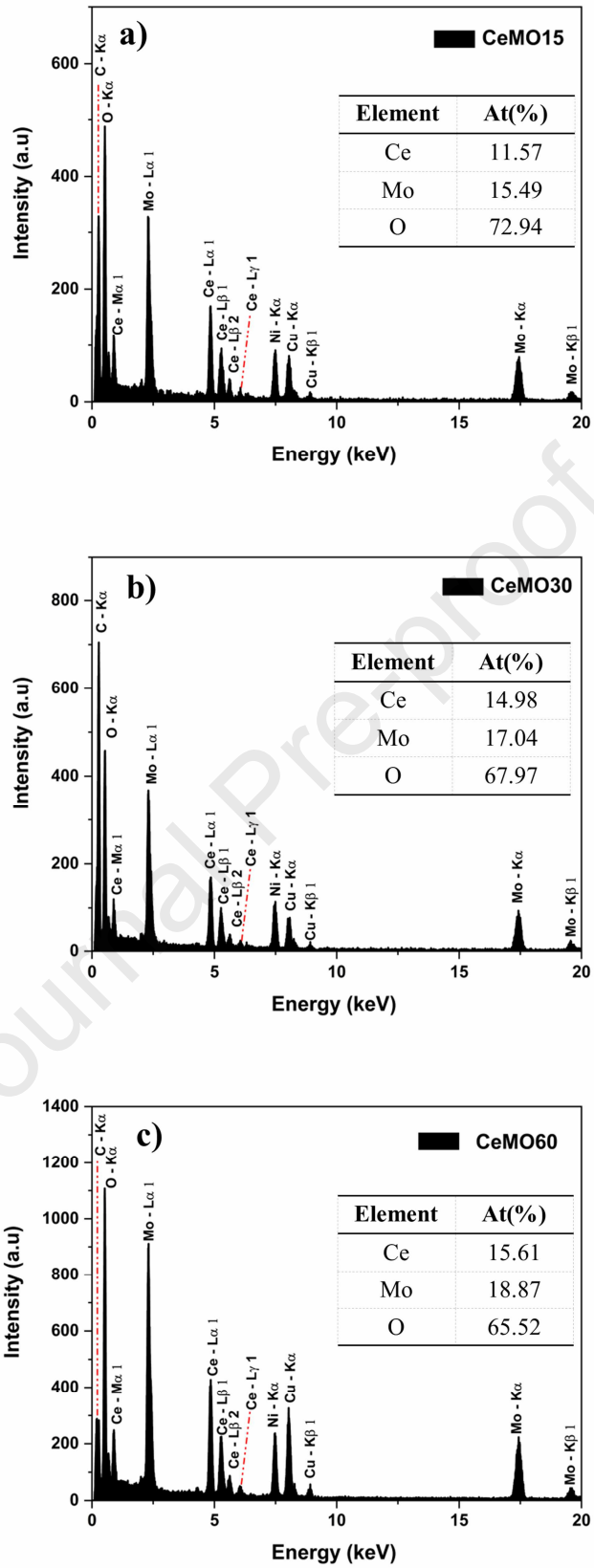

<Fig. 6>

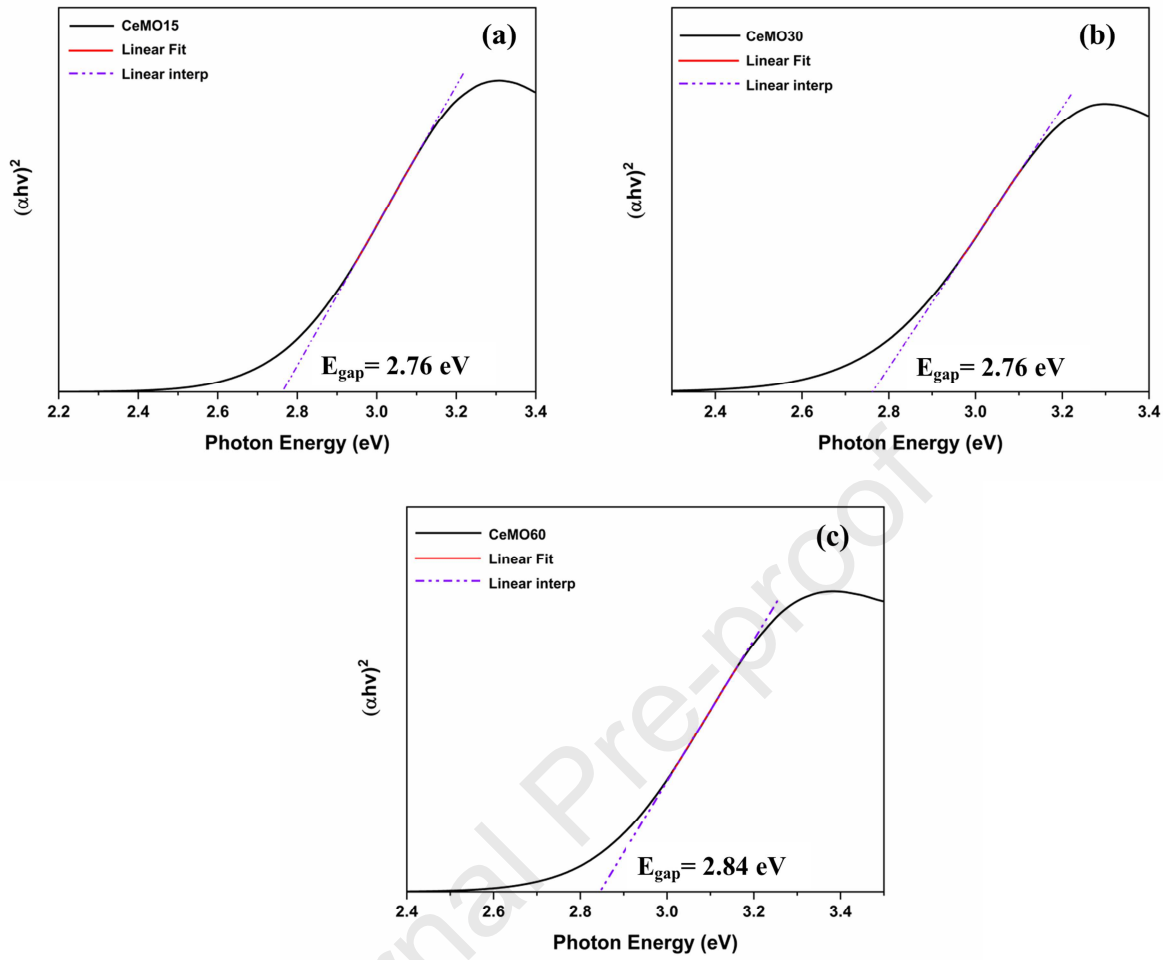

<Fig. 7>

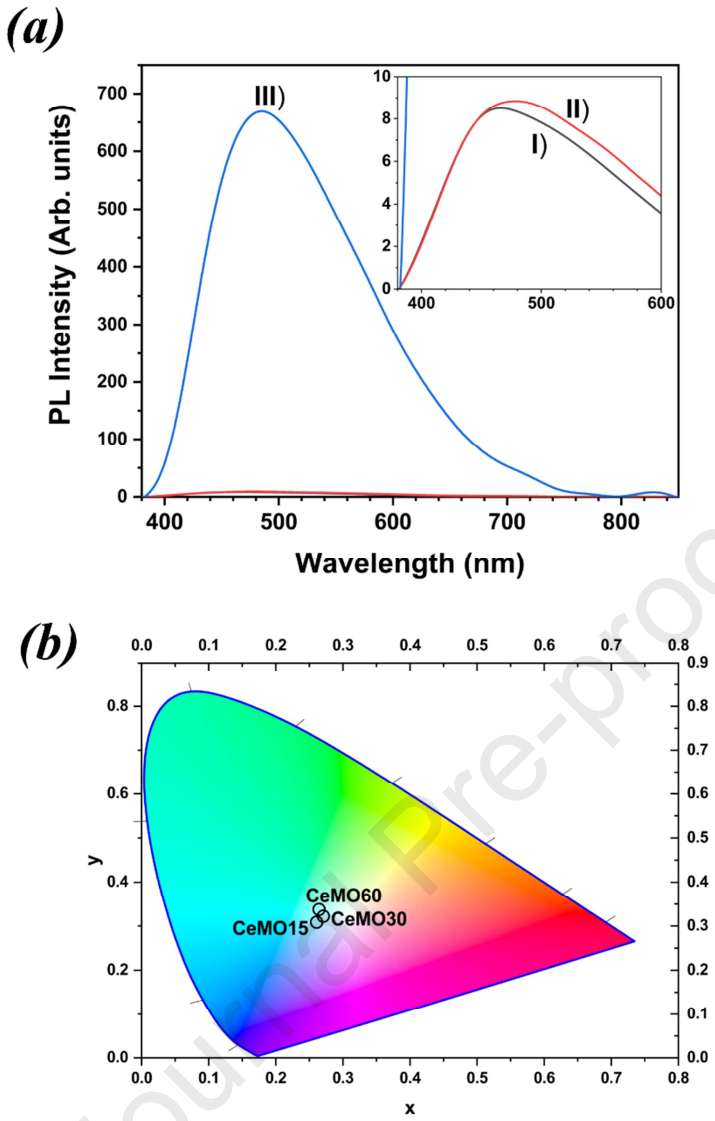

<Fig. 8>

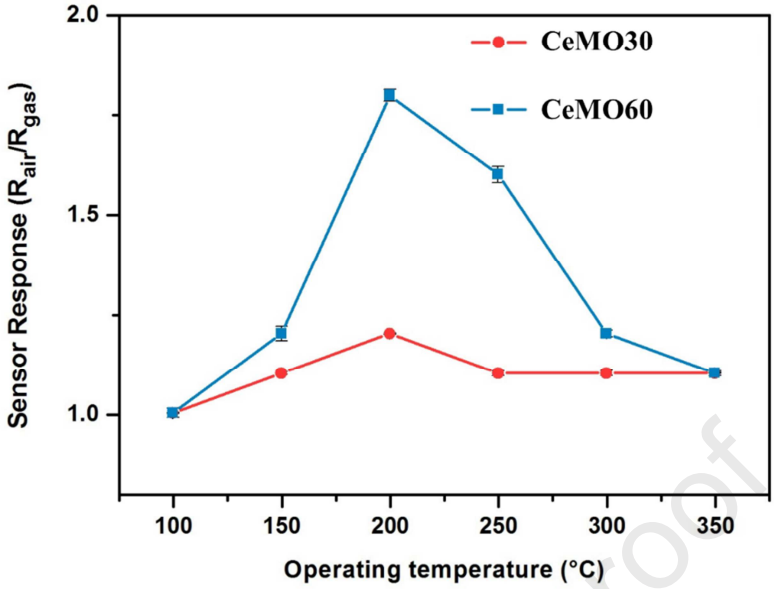

<Fig. 9>

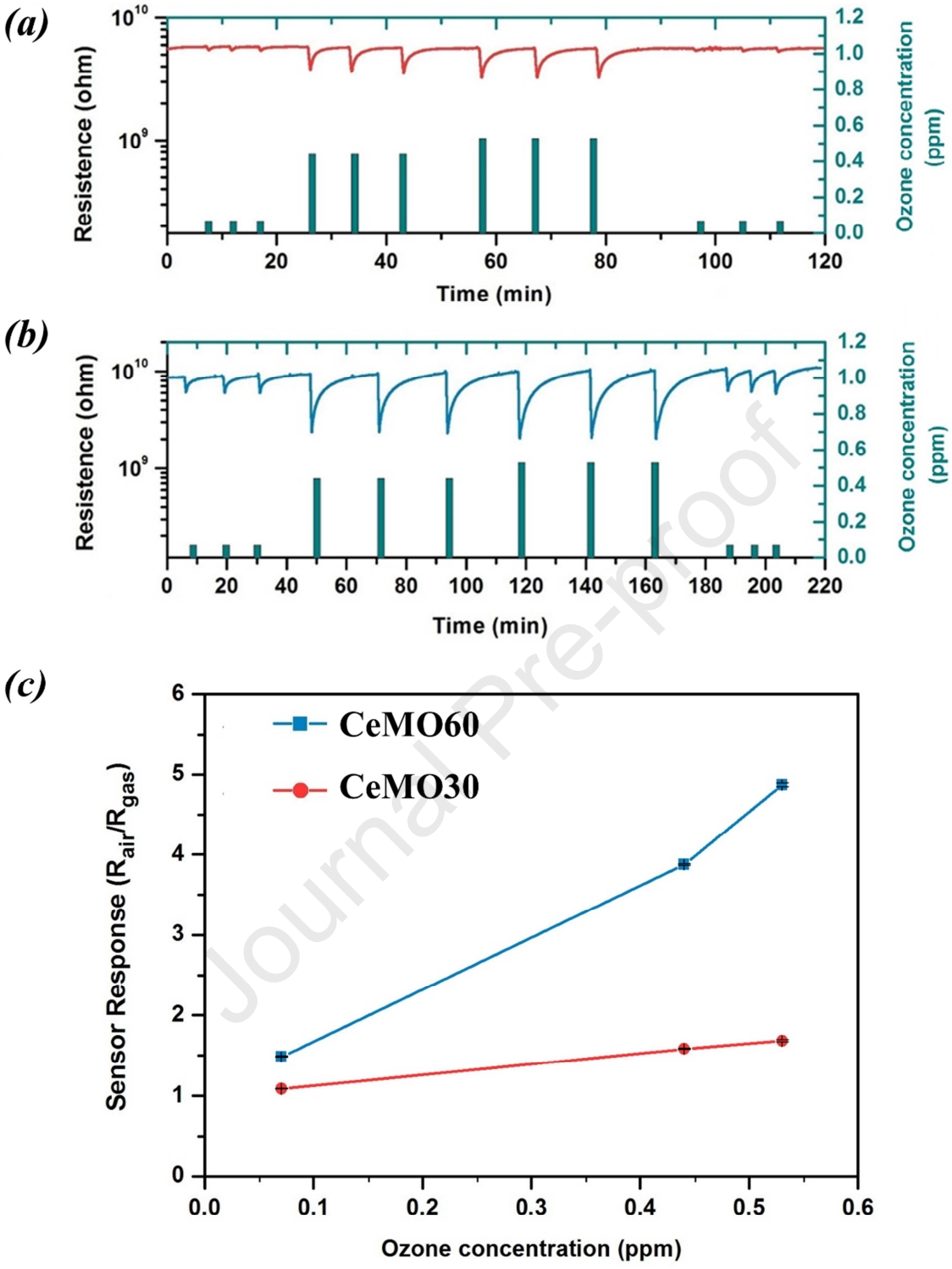

<Fig. 10>

Highlights

- $Ce_2(MoO_4)_3$ samples were obtained by microwave-assisted hydrothermal method.
- $Ce_2(MoO_4)_3$ powders exhibited potentiality like ozone gas sensor materials.
- Gas-sensing experiments revealed a good sensitivity of $Ce_2(MoO_4)_3$ samples.
- Ozone gas in the range of 0.07 to 0.53 ppm, exhibiting total recovery.

Declaration of interests

☒ The authors declare that they have no known competing financial interests or personal relationships that could have appeared to influence the work reported in this paper.

☐The authors declare the following financial interests/personal relationships which may be considered as potential competing interests: